

UNIVERSITAT DE BARCELONA
DEPARTAMENT D'ASTRONOMIA I METEOROLOGIA



Determination of the distance to the Andromeda Galaxy using variable stars

Memòria presentada per
Francesc Vilardell Sallés
per optar al grau de
Doctor en Física

Barcelona, gener de 2009

2 Time series photometry★

The main goal of this project (Sect. 1.4) requires high-quality light curves to obtain precise fundamental properties. By the time this project started, the highest-quality EB light curves were those obtained by the DIRECT group (Kaluzny et al., 1998; Stanek et al., 1998, 1999), but the scatter was too large to determine the physical elements reliably (see Sect. 1.3.3). Therefore, we undertook a new photometric survey to obtain high-quality EB light curves (see Sect. 2.1). With the application of the difference image analysis algorithm in the data reduction process (see Sect. 2.2), precise photometry was obtained not only for the EBs in the field, but also for all the variable stars. Two photometric catalogs were compiled (see Sect. 2.3). The reference catalog contains the photometry in both B and V passbands of 236 238 stars. Among all the stars in the reference catalog, 3 964 were identified as variable and included in the variable star catalog. The variable star catalog contains 437 EBs and 416 Cepheids and represent the initial lists of variable stars used for distance determination to M 31.

2.1 Observations

The observations were conducted at the 2.5 m Isaac Newton Telescope (INT) in La Palma (Spain). Twenty-one nights in five observing seasons were granted between 1999 and 2003 (one season per year). The Wide Field Camera, with four thinned EEV 4128×2148 CCDs, was used as the detector. The field of view of the WFC at the INT is $33'8 \times 33'8$, with $0''.33 \text{ pixel}^{-1}$ angular scale. With this configuration, we found that an exposure time of 15 minutes provides the optimum S/N for stars of $V \sim 19$ mag and ensures that no significant luminosity variation occurs during the integration for EBs with a period longer than one day.

All observations were centered on the same field located in the north eastern part of M 31 ($\alpha = 00^{\text{h}}44^{\text{m}}46^{\text{s}}$ $\delta = +41^{\circ}38'20''$). The field of study (Fig. 1.5) was

*The contents of this chapter were published in Vilardell et al. (2006).

Table 2.1. Number of images used in the data reduction process for each of the five observing campaigns.

Frame	1999	2000	2001	2002	2003	Total
Granted nights	3	4	4	5	5	21
Bias	5	21	10	46	24	106
Darks	0	0	0	6	0	6
<i>B</i> flat-fields	20	31	19	21	42	133
<i>V</i> flat-fields	23	17	14	27	25	106
<i>B</i> Landolt fields	12	0	8	0	0	20
<i>V</i> Landolt fields	16	0	11	0	0	27
<i>B</i> M 31 field	41	45	45	54	80	265
<i>V</i> M 31 field	40	45	43	49	82	259
Total	157	159	150	203	253	922

selected to overlap with the DIRECT fields A, B, and C, since the initial main objective of the project was to obtain high-quality photometry of already known EBs (see Sect. 1.4). To reduce blending problems in such a crowded field (see Fig. 2.1), all the images with PSF FWHM larger than $3''$ were rejected. As a result, 265 and 259 frames, with median seeings of $1''.3$ and $1''.2$, were selected for further analysis in the *B* and *V* passbands, respectively. In addition, during two nights of the 1999 observing run and one night of the 2001 observing run, 15 Landolt (1992) standard stars were observed from three fields (PG0231+051, PG1633+099, and MARK A). In Table 2.1, a complete list of all the images used in the data reduction process for the five observing seasons is presented.

2.2 Data reduction

The treatment of the obtained images follows five major steps: (1) raw data calibration to correct the images, (2) difference image analysis to obtain differential photometry for the variable stars, (3) standard photometry transformation, (4) astrometry to obtain the star positions and (5) periodicity search to compute the periodicity for the variable stars.

2.2.1 Data calibration

The science images for each of the five observing seasons were reduced using the IRAF¹ package. Only bias, dark, and flat-field frames corresponding to the same

¹IRAF is distributed by the National Optical Astronomy Observatories, which are operated by the Association of Universities for Research in Astronomy, Inc., under cooperative agreement with the NSF.

observing season were used to reduce a given science image.

Each WFC image was separated into four overscan-subtracted images, one per CCD frame. After this step, each CCD frame was treated separately during the reduction process. Bad pixels² were also corrected for all images through linear interpolation from the adjacent pixels. Although this method is not optimal for reducing photometric data (since the flux of stars on bad columns is not conserved), it yields the best results for cleaning the calibration images (bias and flat-field images).

A master bias was built for each observing season and CCD frame. Each pixel of the master bias is the median value of the same pixel in all the bias frames. The resulting bias frames were subtracted from each flat-field frame. The bias-subtracted flat-field frames were corrected for non-linearity effects³ and averaged to produce a master flat-field image for each observing season, CCD frame, and filter.

The science images were processed by subtracting the bias frame and corrected for non-linearity and flat fielding. The resulting images are free of most of the instrumental effects, except for a small area close to the north eastern corner of the field that is associated with field vignetting (see Fig. 2.1).

2.2.2 Difference image analysis

Given that the field under study is highly crowded, a package based on the image subtraction algorithm (Alard & Lupton, 1998) was used to obtain the best possible photometric precision. This technique has the advantage that variable stars are automatically detected and that precise photometry can be obtained even in highly crowded fields. We used our own implementation of the difference image analysis package (DIA) developed by Wozniak (2000). The image subtraction algorithm requires a high-quality reference image. This image was created during the first step of the process by the DIA for each CCD and filter. The combination of the 15 best seeing images produced two reference images, one with 0".9 FWHM for *V* (see Fig. 2.1) and one with 1".0 FWHM for *B*.

The main part of the process is the determination of the convolution kernels. The kernels are constructed to match the reference image with each one of the remaining frames under study (supposedly with different seeing values). The DIA kernels are composed of Gaussian functions with constant widths and modified by polynomials. In our case, the kernels consist of three Gaussians with polynomials of orders 4, 3, and 2. A space-varying polynomial of order 4 was also used to

²The pixel positions were obtained from the webpage:
<http://www.ast.cam.ac.uk/~wfcsur/technical/pipeline/>

³Coefficients were obtained from the webpage:
<http://www.ast.cam.ac.uk/~wfcsur/technical/foibles/>

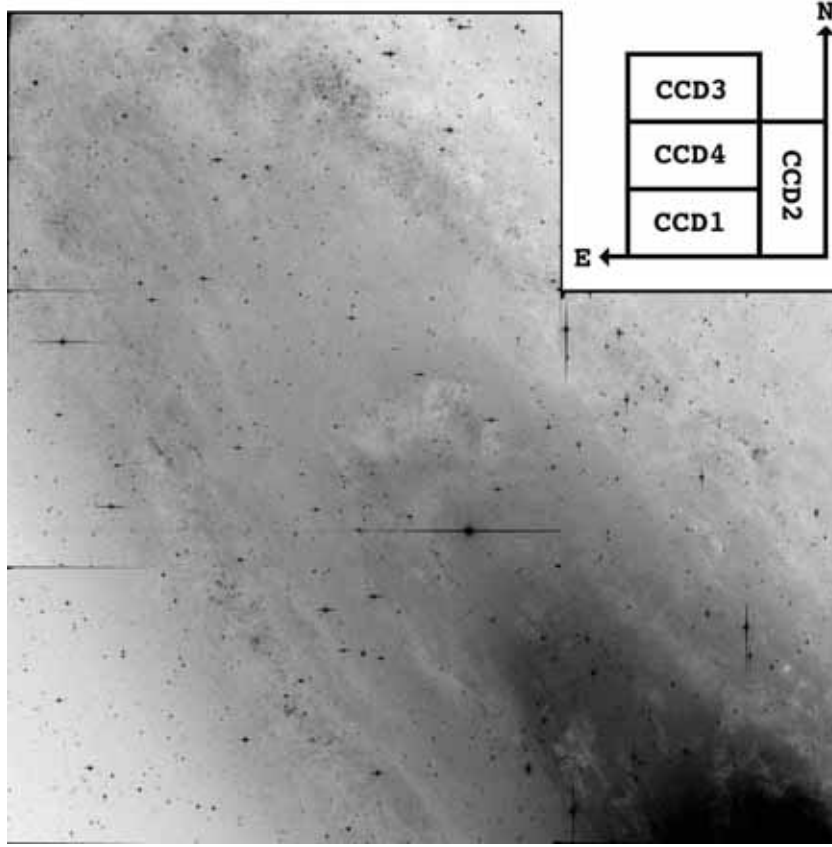


Figure 2.1. Reference image of the selected field of view in V filter. The center of the field is at $\alpha = 00^{\text{h}}44^{\text{m}}46^{\text{s}}$ and $\delta = +41^{\circ}38'20''$

account for the spatial variation across the image. The resulting kernels were convolved with the reference image and subtracted from the original frames to obtain images containing only objects with brightness variations (plus noise).

The variability image is constructed from the differentiated images. This variability image contains all pixels considered to have light-level variations. A pixel is considered to vary if it satisfies at least one of the following two conditions:

- There are more than 4 consecutive observations deviating more than 3σ (where σ is the standard deviation) from the base-line flux in the same direction (brighter or fainter).
- There are more than 10 overall observations deviating more than 4σ from the base-line flux in the same direction.

The variability image is used to identify the variable stars. The reference image PSF is correlated with the variability image and all local maxima with correlation coefficients in excess of 0.7 are considered to be variable stars. Once the

variable stars are located, PSF photometry is performed on all the differentiated images to obtain the differential fluxes. The differential fluxes can be transformed to the usual instrumental magnitudes through the following expression:

$$m_i = C - 2.5 \log(f_0 + a\Delta f_i) \quad (2.1)$$

where Δf_i is the differential flux of a star in the i th observation, f_0 is the base line flux on the reference image, C is a zero-point constant, m_i is the instrumental magnitude of a star in the i th observation, and a is a scaling factor (see below).

The photometric package of DIA does not properly account for contamination from nearby stars in crowded fields (such as in our case). Therefore, the f_0 values obtained with the DIA can potentially be severely overestimated. To obtain precise values for f_0 , DAOPHOT PSF photometry (Stetson, 1987) was applied to the reference image. Given that DIA and DAOPHOT photometry use different PSF definitions and functional forms, a scaling factor (a) is needed to transform the DIA fluxes into the DAOPHOT flux units (see Zebrun et al., 2001, for an extensive discussion). A synthetic image was created to compute the scaling factors. The synthetic image contains the representation of the DAOPHOT PSFs at the position of each variable star. The scaling factor at the position of each variable star was obtained from the comparison with the DIA photometry of each PSF. For similar PSFs, the scaling factor can be obtained with an error of 0.3% or less.

This process provided instrumental magnitudes for all the variable stars, as well as all the stars in the reference image. Two main sources of potential systematic errors exist with this procedure, f_0 and a . Both sources affect the amplitudes of the light curves without introducing any additional scatter. Therefore, the only way to study the presence of possible systematics is by comparing the derived light curves with other results given in the literature. As shown in Sect. 2.4.1, the amplitudes of the fitted EBs are perfectly compatible with DIRECT light curves. In addition, the reference fluxes (f_0) result in standard magnitudes that are fully compatible with LGGS and DIRECT standard magnitudes (Sect. 2.3.1). Therefore, the existence of any additional photometric errors resulting from systematics in the derived parameters (f_0 and a) can be excluded.

2.2.3 Standard photometry

To transform instrumental to standard magnitudes, the observed Landolt (1992) standard stars were used. Although the standard stars were observed at different times during the night, the number of collected frames is not enough to accurately determine the atmospheric extinction. Therefore, as a first step, the M 31 images obtained during the same night as the standard stars (30 images in total) were used to compute the coefficients needed to account for the atmospheric extinction. Aperture photometry on 20 bright, but not saturated, and isolated stars on the

M 31 frames was performed. For each night and filter, a linear fit was obtained with dispersions ranging from 0.008 mag to 0.03 mag.

As a second step, aperture photometry was performed on the standard stars. The instrumental magnitudes obtained were corrected with the atmospheric extinction coefficients. The resulting values were used to find the transformation coefficients between the instrumental magnitudes and the standard magnitudes. For each night and CCD, the following relationship was determined:

$$v - V = A_1 + A_2(B - V) \quad (2.2)$$

$$b - v = A_3 + A_4(B - V) \quad (2.3)$$

where b and v are the instrumental magnitudes, B and V the standard magnitudes, and A_i are the transformation coefficients. The resulting mean standard deviation of the fits is 0.02 mag.

The transformation coefficients cannot be directly applied to the M 31 instrumental magnitudes because the latter are based on the reference image, which is a combination of different images. In addition, the transformation coefficients are determined from aperture photometry, while the M 31 instrumental magnitudes have been determined from PSF photometry. For this reason, the only way to obtain standard magnitudes for the M 31 stars is to apply the transformation coefficients to the frames obtained during the same nights as the standard stars.

PSF photometry is needed to find precise standard magnitudes of a reasonable number of objects in the M 31 field, since aperture photometry can only be applied to isolated stars. A sample of bright and isolated stars was used to determine a scaling value to transform the PSF magnitudes into aperture photometry values for each one of the 30 M 31 frames. The scaling values and the transformation coefficients were then used to obtain standard magnitudes for 18 426 objects in the field. A systematic difference was observed for the standard magnitudes obtained from the 2001 frames (probably the night was not photometric), so these values were rejected. The standard magnitudes of every star in all the remaining frames (22 in total) were averaged, and the standard deviation was considered a good estimation of its uncertainty.

The standard magnitudes resulting from this process were used to determine new transformation coefficients (A_i) for the reference images. Only 534 non-variable and non-saturated objects detected in all the frames and with an error below 0.04 mag were used for this purpose. This sample has good standard color and magnitude coverage, with $-0.3 < B - V < 1.7$ mag and $17.5 < V < 21.0$ mag, providing fits with dispersions ranging from 0.013 mag to 0.019 mag, depending on the CCD.

The resulting coefficients were applied to the reference images. The objects detected in the V frame were cross-matched with the objects detected in the B frame. Only the objects identified within $0''.33$ (one pixel) in *both passbands* have

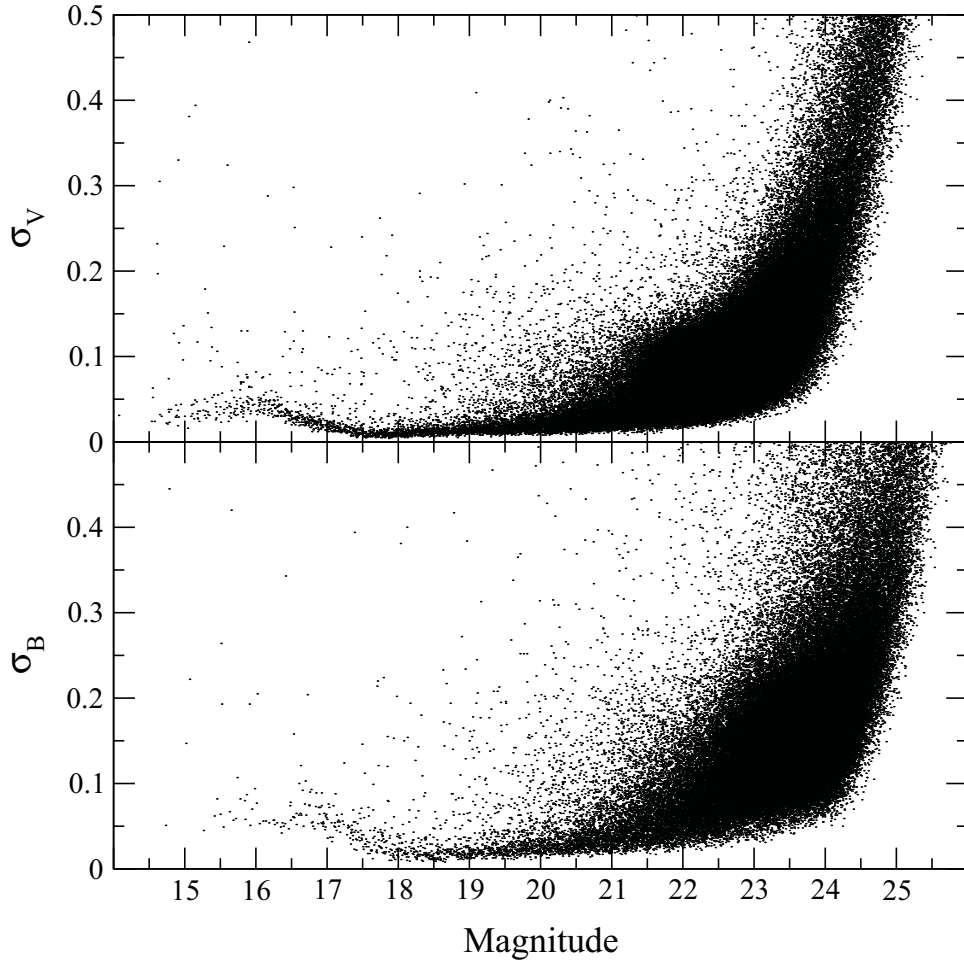


Figure 2.2. Standard errors as a function of magnitude for the entire photometric catalog containing 236 238 objects with photometry in both V and B passbands.

been included in the reference catalog, providing standard photometry for 236 238 objects. Of these, 37 241 objects have errors below 0.1 mag in both passbands (Fig. 2.2). The limiting magnitudes of the photometric catalog are around $V \simeq 25.5$ mag and $B \simeq 26.0$ mag, and it is estimated to be complete up to $V \simeq 22.3$ mag and $B \simeq 23.5$ mag (see Fig. 2.3). Including only the objects with photometry in both passbands introduces a bias in the V band completeness because stars usually have positive $B - V$ values. Therefore, some faint stars in V were not included in the catalog because their B magnitudes were beyond the detection limit. Since the standard color is needed to obtain the V standard magnitude, this procedure ensures that all the photometry in the reference catalog uses the same transformation coefficients.

Finally, the same coefficients used in the reference images were applied to transform the m_i values in Eq. 2.1 to standard photometry in both B and V passbands for a total of 3 964 variable stars.

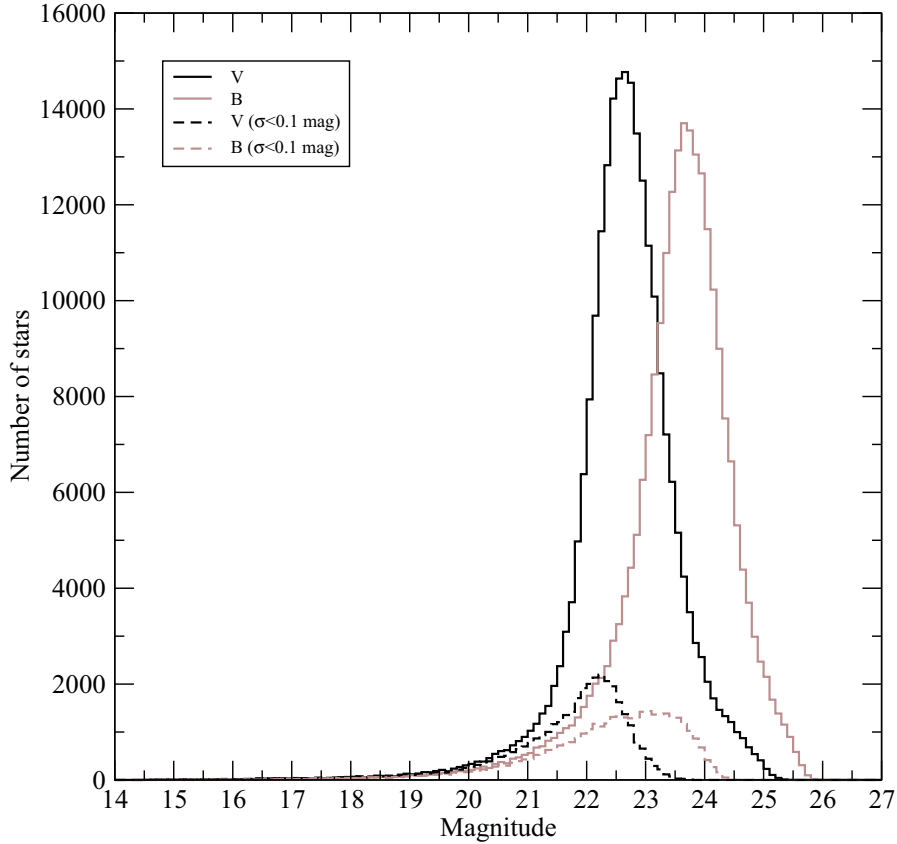


Figure 2.3. Number of stars as a function of the standard magnitudes for the two passbands (B and V). Number of stars with errors below 0.1 mag are also shown.

2.2.4 Astrometry

Standard coordinates for all detected objects were computed from several reference stars in the GSC 2.2.1⁴. To ensure that the reference stars are uniformly distributed, each CCD was divided into 3×6 sectors. Three reference stars (with $V \simeq 18$) were identified manually in each sector, yielding an initial list of 54 reference stars per CCD. Fits using third-order linear equations with 2σ scatter clipping were applied to determine the transformation of coordinates. After the iterative process, at least two reference stars had to remain in each sector. Otherwise, an additional reference star was selected in the corresponding sector and the entire process was repeated.

The resulting coordinates were compared with those in the GSC 2.2.1 catalog. A total of 724 objects with a position difference of less than $3''$ in the two catalogs were identified. As can be seen in Fig. 2.4, no systematic trends appear in the comparisons, which have dispersions of $\sigma_\alpha = 0''.16$ and $\sigma_\delta = 0''.12$.

⁴Data obtained from: <http://cdsweb.u-strasbg.fr/viz-bin/Vizier>

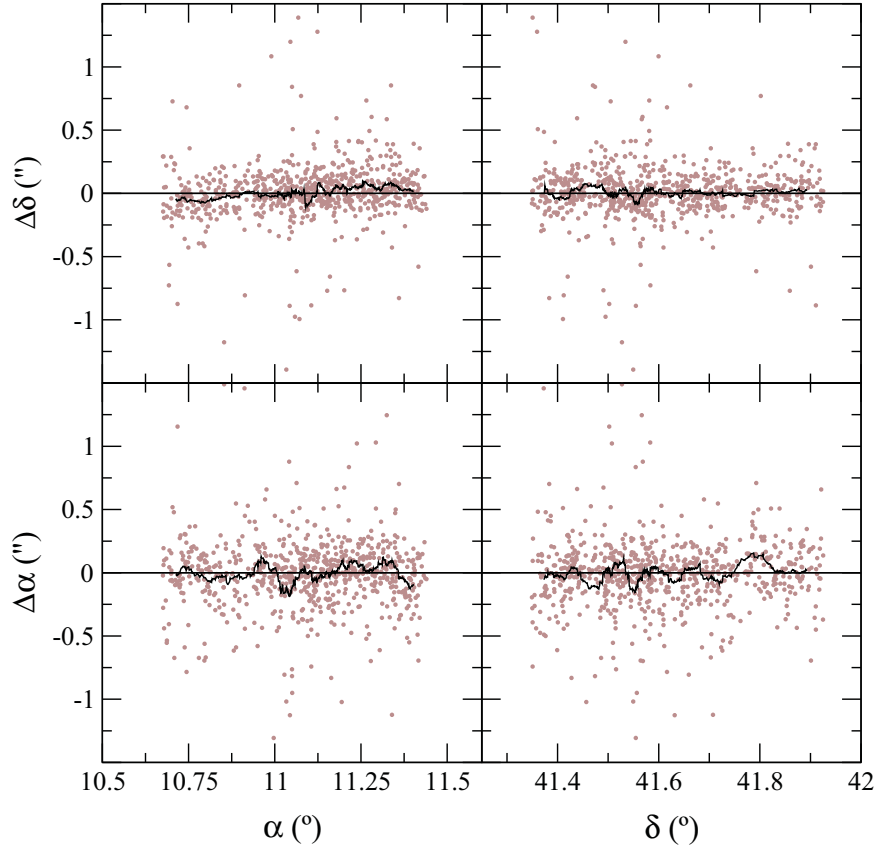


Figure 2.4. Differences between the coordinates obtained from our procedure and the coordinates from the GSC 2.2.1 catalog for 724 identified stars (circles). The line represents a running average.

2.2.5 Periodicity search

Since the observations were performed in five annual observing seasons, the data are very unevenly sampled. To overcome this major drawback in determining periodicities, a program based on the analysis of variance (Schwarzenberg-Czerny, 1996) was used to compute the periodograms for each variable star and filter (B and V). The periodograms were computed with 7 harmonics, because this setup was found to provide optimal results for the detection of EB systems, which constitute the main objective of the present survey. The lower limit in the period search was set to one day from the consideration that EBs with periods below one day are likely to be foreground contact systems and therefore not of interest for this survey. In addition, given the relatively long exposure time for each observation in the present survey (15 minutes), important brightness variations during the integration time could occur for the short-period variables. These factors make the computational effort of extending the period search below 1 day not worthwhile. On the opposite end, an upper limit of 100 days was selected to detect as many

long-period Cepheids as possible.

For each variable star, two periodograms (one in B and one in V) were used to obtain a consistent period determination. The resulting light curves were visually inspected to locate well-defined variability patterns, thus leading to the identification of a total of 437 EBs and 416 Cepheids. For several EBs and Cepheids, the period determination was a multiple of the true period and, therefore, it was recomputed. Finally, the times of minimum of both light curves (B and V), which were computed from Fourier series ($F^{(7)}(t)$ in Schwarzenberg-Czerny, 1996), were used to compute a reference time for all the light curves.

2.3 The catalogs

As a result of the data reduction process, two catalogs were obtained. The first one includes all the detected objects in the field. The second one contains the data for all the variable stars.

2.3.1 Reference catalog

The photometry of the 236 238 objects detected in the reference images was grouped into the reference catalog (Table 3)⁵, which contains the object identifier, the right ascension, the declination, the V standard magnitude in the reference image, the V standard error, the B standard magnitude in the reference image, the B standard error, and, in case there is a previous identification, the corresponding identifier. The catalogs cross-matched with our reference catalog are GSC 2.2.1, DIRECT, LGGS (Massey et al., 2006), and Todd et al. (2005, hereafter T05). Photographic catalogs are identified in the previous works, specially in LGGS, and they are not cross-identified here.

According to the IAU recommendations, the identifier was built from the object position and considering the observational angular resolution. The resulting format is M31 JHHMMSSss+DDMMSSs. For the variable stars, the acronym was changed from M31 to M31V to indicate that they can be found (with the same identifier) in the variable star catalog (see Sect. 2.3.2).

To show the general photometric properties of the obtained catalog, the color-magnitude diagram for the 37 241 objects with a photometric error below 0.1 mag in both B and V is shown in Fig. 2.5. It can be seen from this diagram that most of the stars in this catalog are stars at the top end of the main sequence, with some foreground giants and stars at the tip of the red giant branch.

⁵Table 3 is available in electronic form at the CDS via anonymous ftp to cdsarc.u-strasbg.fr (130.79.128.5) or via <http://cdsweb.u-strasbg.fr/cgi-bin/qcat?J/A+A/459/321>

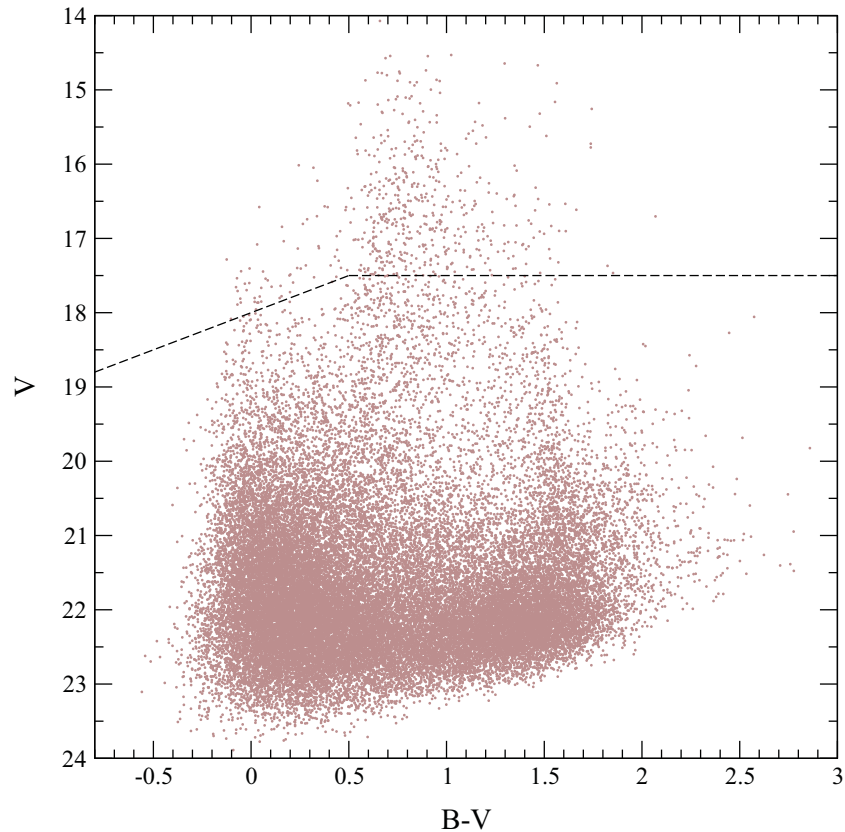


Figure 2.5. Color–magnitude diagram for 37 241 objects with photometric errors lower than 0.1 mag in both B and V in the reference catalog. Stars above the dashed lines are saturated.

The standard photometry depends on a certain number of zero-point calibrations (Sect. 2.2.2 and Sect. 2.2.3). Considering that an error in the standard magnitudes has a direct impact on the distance determination, it is extremely important to ensure that no systematic errors affect the photometry. For this reason, it is worthwhile checking the consistency of the standard magnitudes given here. Fortunately, there are two CCD surveys with B and V photometry of a large number of stars that overlap with the field under study: DIRECT (Macri, 2004) and LGGS (Massey et al., 2006). The non-saturated objects of our survey ($V > 17.5$ and $B > 18.0$) were cross-identified with the magnitudes reported by the DIRECT group⁶ and by the LGGS group⁷. For the DIRECT survey, a total of 14 717 and 7 499 objects were identified in V and B passbands, respectively (see Fig 2.6). The comparison with the LGGS survey provided 36 353 common objects (see Fig. 2.7).

Although some trend is observed for the DIRECT B magnitudes, the LGGS B

⁶Data source: <ftp://cfa-ftp.harvard.edu/pub/kstanek/DIRECT/>

⁷Data source: <http://www.lowell.edu/users/massey/lgsurvey/>

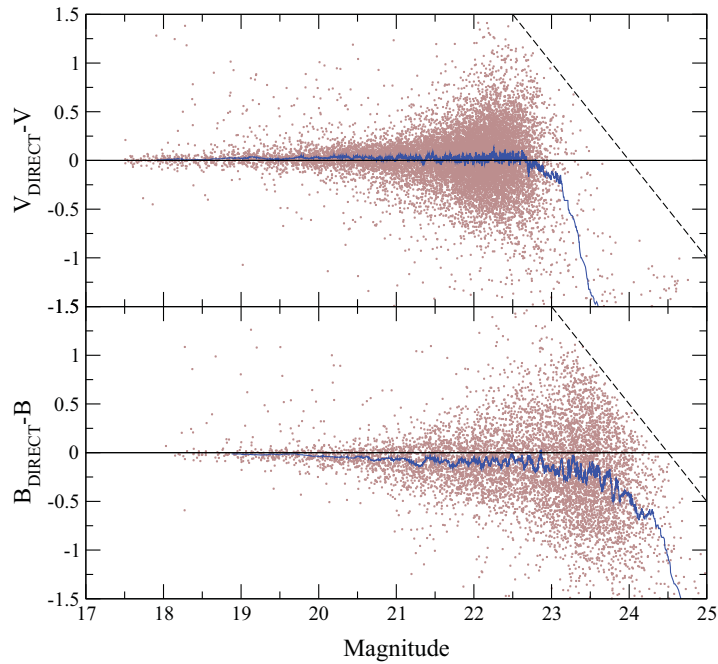


Figure 2.6. Differences with DIRECT standard magnitudes versus the magnitudes in the reference catalog. The comparison has 14 717 stars in V and 7 499 in B . The dashed lines show the limiting magnitudes. The solid line is a running average.

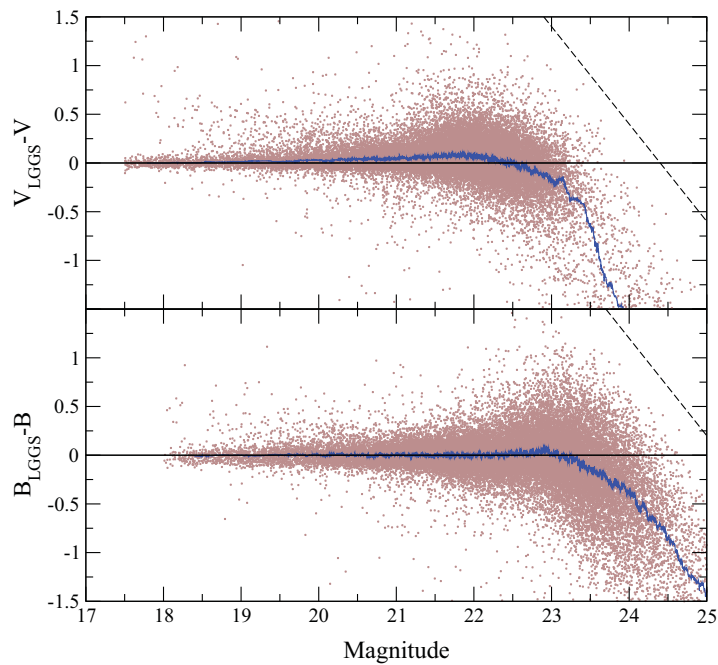


Figure 2.7. Differences with LGGS standard magnitudes versus the magnitudes in the reference catalog for a total amount of 36 353 stars in each passband. The dashed lines show the limiting magnitudes. The solid line is a running average.

magnitudes are completely consistent with the magnitudes in our survey. Therefore, the B standard magnitudes in the present catalog are expected to have no systematic error. Regarding the V magnitudes, some low-level systematics have been observed with the two catalogs. The DIRECT V magnitudes are larger by about 0.02 mag than the values in the reference catalog, and the LGGS comparison shows an increasing trend towards larger magnitudes. The 5 768 objects with V magnitudes in the three catalogs were used to study the observed systematics. The comparisons between the three catalogs always reveal some kind of trend and, so it was impossible to conclude whether there are any (low-level) systematics affecting the V standard magnitudes. In any case, the differences for the brightest stars ($V < 20.5$ mag) are well below 0.03 mag. Taking into account that all the EBs that can be used for distance determination have $V < 20.5$ (Sect. 2.4.1), this is the maximum systematic error that can exist in their V standard magnitudes.

2.3.2 Variable star catalog

The 3 964 variable stars identified in the reduction process were included in the variable star catalog (Table 4)⁸. For each variable star, we provide the corresponding identifier (see Sect. 2.3.1), the right ascension, the declination, the intensity-averaged V magnitude (Eq. (9) in Saha & Hoessel, 1990), the mean V error, the intensity-averaged B magnitude, the mean B error, the number of observations in V , the number of observations in B , the reference time computed in Sect. 2.2.5 (in HJD), the period (in days) and a label, indicating whether the variable star was identified as an EB or a Cepheid.

Although a period estimate is given for each variable star, obviously not all the variable stars are periodic. When comparing the window function with the period distribution for all variable stars (see Fig. 2.8), it is clear that many of the period determinations are just an alias introduced by the window function, especially for those over five days (frequency below 0.2 days^{-1}). Therefore, a significant number of the variable stars are, in fact, non-periodic variables or variables with a period out of the studied range (1–100 days). All light curves (time series photometry) are also provided (Table 5)⁹, together with the variable star catalog. For each variable star and observation, the time of observation (in JD), the standard magnitude (V or B) and the standard error are given.

Part of the images in the present survey were also reduced by T05 who reported 127 EB systems. Therefore, the photometry on the variable star catalog

⁸Table 4 is available in electronic form at the CDS via anonymous ftp to [cdsarc.u-strasbg.fr](ftp://cdsarc.u-strasbg.fr) (130.79.128.5) or via <http://cdsweb.u-strasbg.fr/cgi-bin/qcat?J/A+A/459/321>

⁹Table 5 is available in electronic form at the CDS via anonymous ftp to [cdsarc.u-strasbg.fr](ftp://cdsarc.u-strasbg.fr) (130.79.128.5) or via <http://cdsweb.u-strasbg.fr/cgi-bin/qcat?J/A+A/459/321>

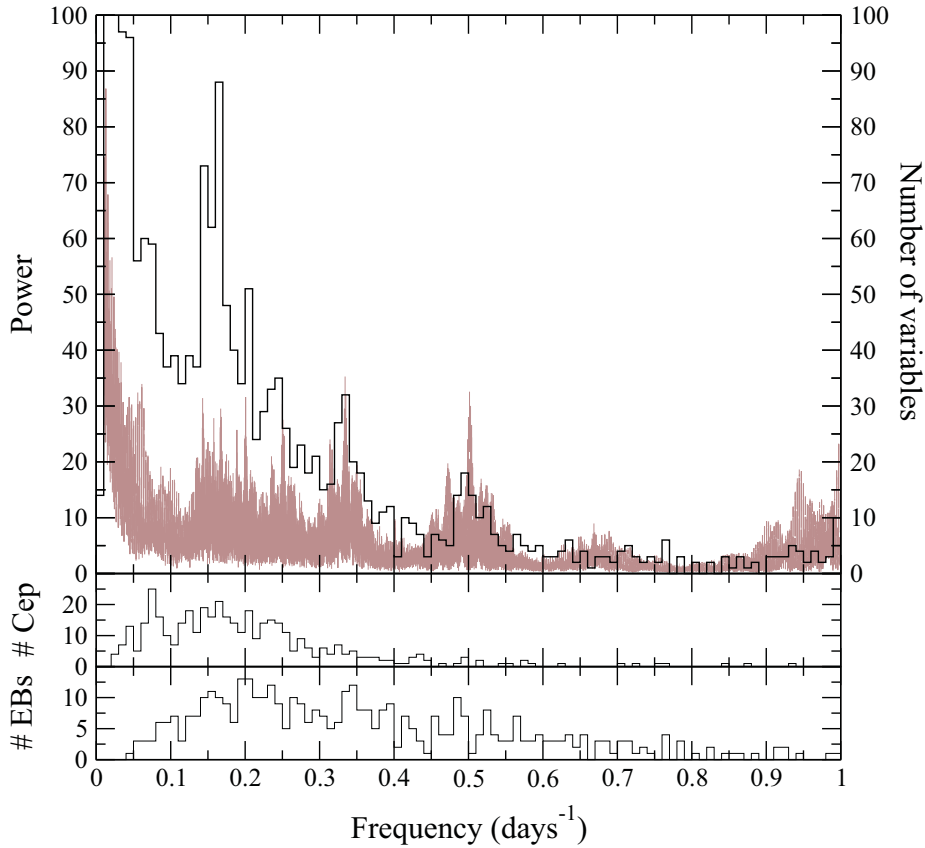


Figure 2.8. **Top:** Window function for the studied period range (lines) and frequency distribution for all the stars in the variable star catalog (histogram). **Middle:** Frequency distribution for the Cepheids in the variable star catalog. **Bottom:** Frequency distribution for the eclipsing binaries in the variable star catalog.

can be directly compared. Of the reported sample of 127 EBs, 123 stars have been detected in our reference catalog, 92 are in the variable star catalog and 90 have also been classified as EBs. The maximum V^{\max} and B^{\max} values for the 90 systems identified were matched with the magnitudes presented in T05 (see Fig. 2.9). A systematic trend can be observed in the V filter. In addition, Fig. 2.9 also reveals that the B_{T05}^{\max} magnitudes are lower than our B^{\max} values.

When inspecting the origin of such a discrepancy, we observed that *all* the EBs labeled f2BEB and f3BEB in T05 had lower magnitude values than the EBs in our variable star catalog. Since 14 of these EBs also have DIRECT V^{\max} magnitudes and 5 of them have DIRECT B^{\max} values (Kaluzny et al., 1998; Stanek et al., 1998, 1999; Bonanos et al., 2003), we computed the mean differences (Table 2.2). Although the number of cross-matched EBs is small, their mean differences seem to indicate that the magnitudes reported in T05 for the f2BEB and f3BEB EBs suffer from a systematic offset. On the other hand, the magnitude values for the remaining EBs (f1BEB and f4BEB) are compatible in the three catalogs.

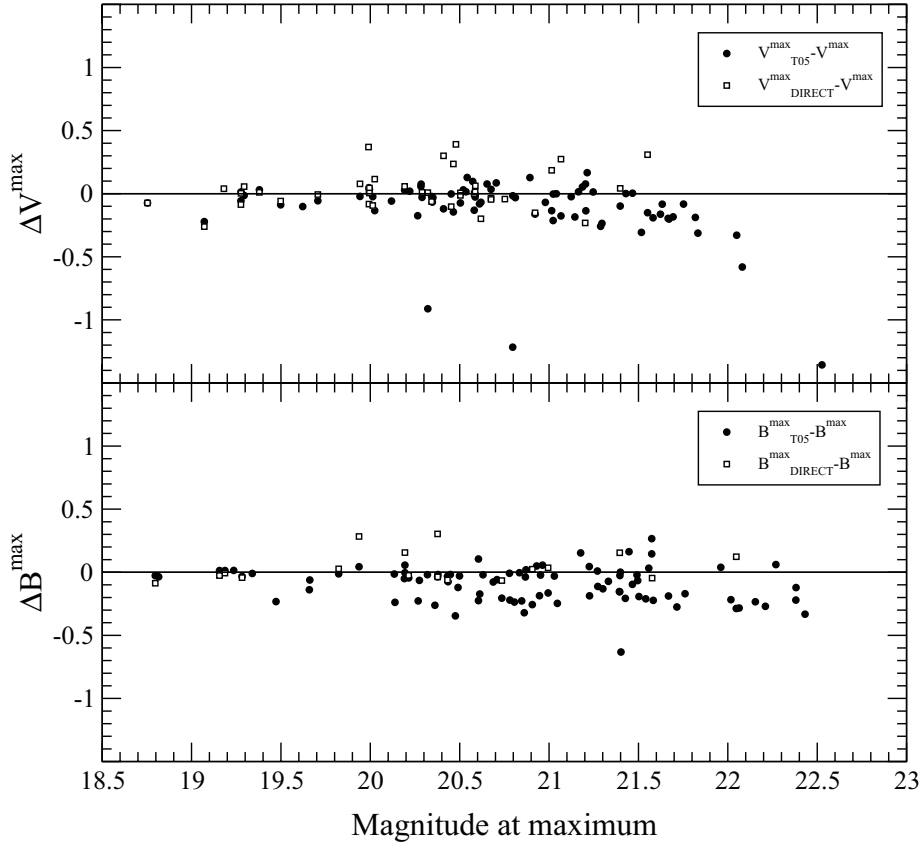


Figure 2.9. Differences between the DIRECT maximum magnitudes (open squares), the T05 maximum magnitudes (filled circles) and the maximum magnitudes for all the crossed EBs of the variable star catalog.

2.4 Selection of variable stars suitable for distance determination

Following the main goal of the present work, the variable star catalog was inspected to identify variable stars suitable for distance determination. Two populations were clearly identified: EBs and Cepheids.

2.4.1 Eclipsing binaries

In order to further characterize the EB sample in the variable star catalog, a neural network algorithm was used (Sarro et al., 2006). After some attempts, it was observed that the neural network still needed some further training to properly classify our EB sample in M 31. Since the training is an arduous effort that demands a large number of well known templates, the classification with neural

Table 2.2. Mean differences for the magnitudes at maximum of the EBs labeled f2BEB and f3BEB in T05.

Comparison	Differences
$V_{\text{DIRECT}}^{\text{max}} - V^{\text{max}}$	0.062 ± 0.047
$V_{\text{T05}}^{\text{max}} - V^{\text{max}}$	-0.104 ± 0.015
$V_{\text{T05}}^{\text{max}} - V_{\text{DIRECT}}^{\text{max}}$	-0.166 ± 0.057
$B_{\text{DIRECT}}^{\text{max}} - B^{\text{max}}$	0.054 ± 0.039
$B_{\text{T05}}^{\text{max}} - B^{\text{max}}$	-0.214 ± 0.026
$B_{\text{T05}}^{\text{max}} - B_{\text{DIRECT}}^{\text{max}}$	-0.268 ± 0.046

networks was withdrawn. Therefore, all the efforts were centered in identifying EBs suitable for distance determination.

Only those systems with a precise determination of their fundamental properties can be used as distance determination targets. In particular, radii with an error of around 4% result in distances with an error larger than 8%, since the absolute magnitude of a star and, hence, the distance, scales as $M_{\text{bol}} \propto R^2$. The absolute radius of a star is obtained from the product of the semi-major axis ($a \sin i$, obtained from radial velocity curves) and the relative radius ($r = R/a$, directly determined from the light curves, Table 1.2). Therefore, an error around 2% is required for each quantity ($\sin i \sim 1$ for EBs). The desired precision in the relative radius can be achieved with photometry on the order of 0.01 mag and the precision in the semi-major axis can be achieved with errors in the semi-amplitudes on the order of 2%. The color–magnitude diagram (see Fig. 2.10) reveals that most of the detected EB systems contain high-mass components on the top of the main sequence. In addition, most of the systems have periods shorter than 10 days (and all of them have periods shorter than 30 days). The expected semi-amplitudes for massive stars with such short periods are on the order of a few hundred kilometers per second. In order to achieve 2% errors in these semi-amplitudes, radial velocities (RVs) with errors on the order of 10 km s^{-1} are required, implying spectral resolutions of $R \sim 3000$ at optical wavelengths. Therefore, considering that medium-resolution spectra are needed to obtain precise fundamental properties and that the largest currently available facilities are the 8–10 m class telescopes, only the brightest EB systems (with $V^{\text{mean}} < 20.5 \text{ mag}$) were selected for further study. In addition, the most precise fundamental properties (such as relative radii) can be achieved only for those systems with deep eclipses, so we further selected only those EBs with $\Delta B \geq 0.2 \text{ mag}$ and $\Delta V \geq 0.2 \text{ mag}$.

The criteria listed above provided a list of 29 systems from the initial sample of 437 EBs. Of these, 5 systems were rejected because of the large scatter in their light curves (probably from the contamination of a brighter nearby star), leaving a total amount of 24 EBs selected for detailed further analysis.

The particular properties of each EB can have a strong influence on the pre-

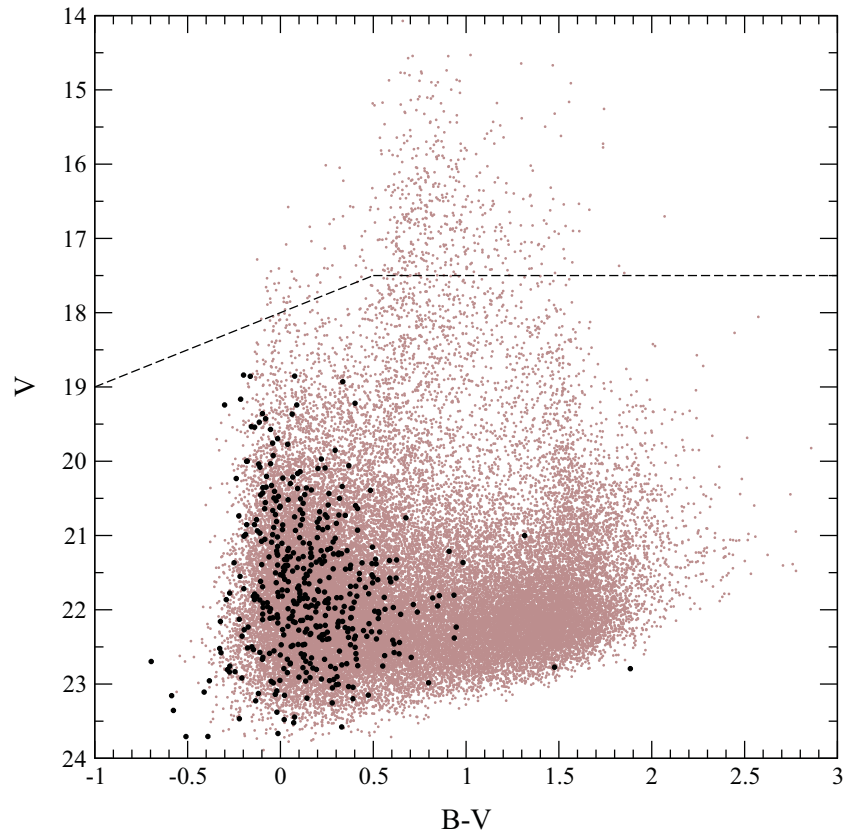


Figure 2.10. Color–magnitude diagram for 37 241 objects with photometric errors lower than 0.1 mag in both B and V in the reference catalog (gray dots) and 437 EBs (black circles). Stars above the dashed lines are saturated.

cise determination of its fundamental parameters. Therefore, to obtain the best distance determination targets, a preliminary fit was performed with the 2003 version of the Wilson & Devinney (1971) program (hereafter W&D) to the selected sample of 24 EBs. The fitting process was carried out in an iterative manner by considering both light curves (B and V) simultaneously. For those systems previously identified by the DIRECT group, their V light curve was also included in the fitting process. This provided an additional check on the consistency of the resulting photometry, because the DIRECT photometry was calculated from a PSF rather than using a DIA algorithm and, therefore, any possible systematics on the DIA photometry (Sect. 2.2.2) can be checked. Once a converging solution was achieved, a 4σ clipping was performed on all the light curves to eliminate (normally a few) outlier observations.

It is important to emphasize that, in the obtained light curves, the primary component has been defined to be the one eclipsed in the primary (deeper) eclipse. This convention has been maintained during the entire work.

In order to obtain more stable solutions, and to decrease the correlation among

the fitted parameters, the W&D assumes a certain configuration for each solution. The different configurations in W&D consider different scenarios where both, one or none of the eclipsing components fill the Roche lobe (the largest closed equipotential around a given star, so there is loss of matter to the companion if one star exceeds its lobe even slightly; Wilson & Wyithe, 2003). As previously mentioned, most of the observed systems seem to be composed by high mass components with relatively short periods. Therefore, a large fraction of the detected EBs are non-detached systems.

Two basic configurations were considered for each EB system: detached and semi-detached. Generally, the final fit in each one of the configurations provided some clues to the real configuration of the EB system. However, all systems showing non-zero eccentricity (secondary eclipse phase not exactly at 0.5) or unequal eclipse widths were considered to be detached EB systems. In some specific cases, a sinusoidal $O - C$ was observed when studying the fit residuals as a function of phase, with one quadrature brighter than the other. This is known as the O’Connell effect (O’Connell, 1951; Davidge & Milone, 1984). In the case of interacting high-mass systems, such effect can be explained by the presence of an equatorial hot spot on the surface of one of the components. This hot spot is supposed to be the consequence of impacting material arising from mass transfer between the components in a Roche-lobe filling configuration (semi-detached). The exact parameters of the spot cannot be obtained from the available data (strong degeneracies exist; Fitzpatrick et al., 2003) and, therefore, the spot parameters presented here are not necessarily physically valid but only capable of providing a good fit to the variations in the light curves.

Each EB needs to be treated as a particular case and careful selection of the adjustable parameters was performed individually. In general, the parameters fitted with W&D for our M 31 EBs are: the time of minimum (t_{\min}), the period (P), the inclination (i), the effective temperature of the secondary ($T_{\text{eff},S}$), the normalized potential of primary (Ω_p), the normalized potential of secondary (Ω_S , for detached systems only), and the luminosity of the primary (L_p). For the eccentric systems, in addition, the eccentricity (e) and the argument of the periastron (ω) were also fitted. In some cases of semi-detached systems, the mass ratio (q) was treated as a free parameter. The limb-darkening coefficients (square-root law) were computed at each iteration from Kurucz ATLAS9 atmosphere models and the gravity brightening coefficients, as well as the bolometric albedos, were fixed to unity (assuming components with radiative envelopes). Finally, a third light (I_3) contribution was included for the final solutions of the EB systems. Since the field under study is extremely crowded, it is not surprising that some EBs may have a significant third light contribution (see Sect. 5.3.3 for a more extensive discussion on this topic). In addition, the obtained values of the third light contribution provide a first check on the realistic determination of the fundamental properties and give an indication of whether the scaling factor determinations (a in Eq. 2.1) are correct. Indeed, an error in the scaling factor has exactly the same effect as a third

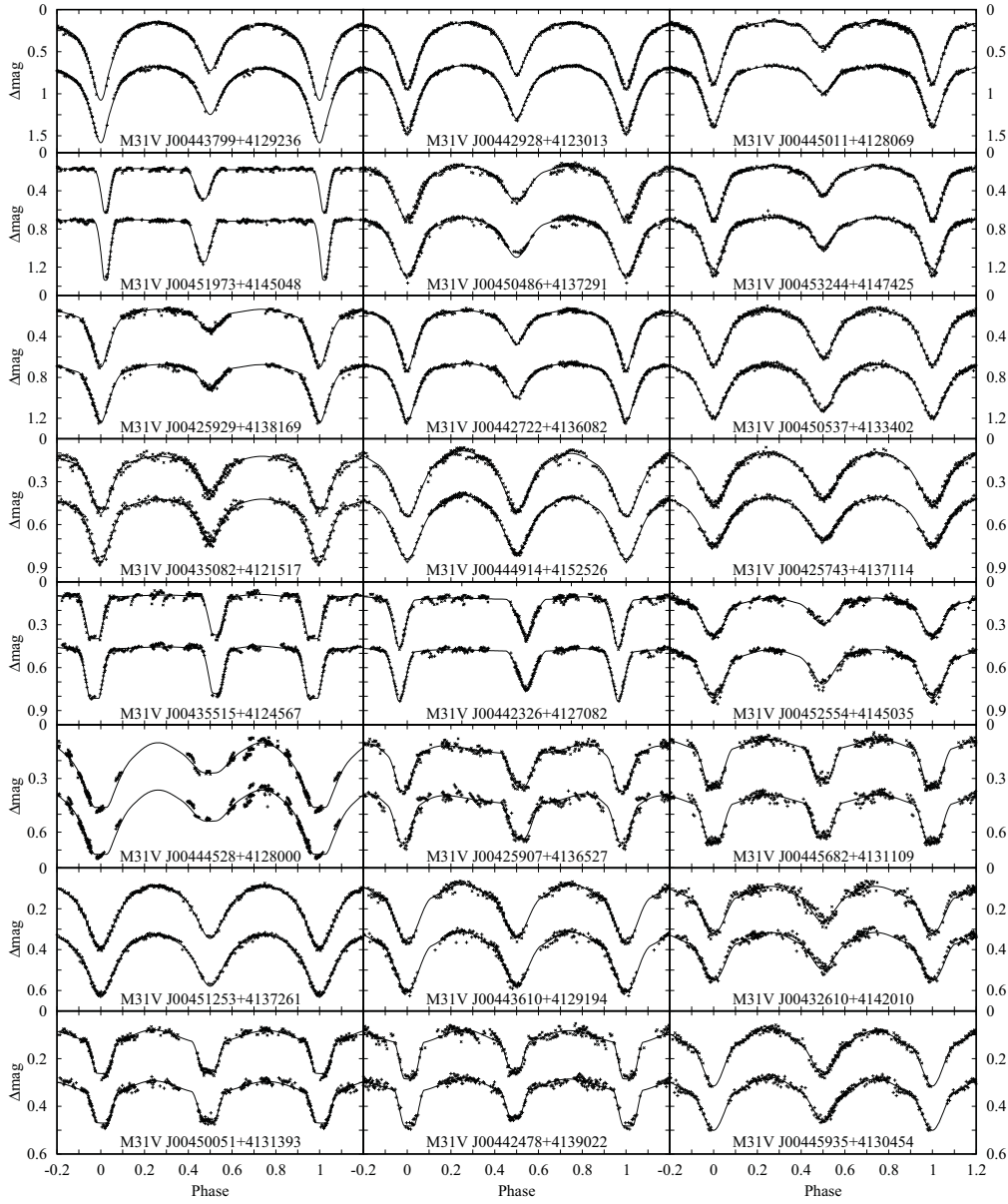


Figure 2.11. B (up) and V (down) light curves for the 24 fitted EBs. The corresponding W&D fits are also plotted (lines).

light contribution (either negative or positive).

Note that most of the solutions have a large number of free parameters. To some extent, the values presented here rely on the adoption of the mass ratio and, therefore, the fit results (in Table 2.3 and Fig. 2.11) should be regarded as preliminary until radial velocity curves are obtained. For some of the binaries, the values given in Table 2.3 need additional comments:

- M31V J00444528+4128000. This is the brightest EB system detected. A

converging fit could not be achieved because of variations in the light curve at the second quadrature. At this point, several possibilities could explain the observed variability, such as a varying hot spot, an accretion disk or the intrinsic variability of a supergiant component. This issue is further discussed in Sect. 4.1.3.

- M31V J00442326+4127082. The DIRECT light curve reveals a variation in the argument of periastron, thus indicating the presence of rapid apsidal motion ($\dot{\omega} = 1.9 \pm 0.6 \text{ deg year}^{-1}$). Even taking the important third light contribution into account, the RV curves provide valuable information for studying the real nature of this detached, eccentric system (Sect. 4.1.4).
- M31V J00443799+4129236. From the fit residuals it became evident that the first quadrature is brighter than the other quadrature by about 0.025 mag in B and 0.020 mag in V . We modeled this effect in W&D by including a hot spot on the primary component. Assuming such a circular spot to be 40% hotter than the photosphere, its predicted radius is $16 \pm 1 \text{ deg}$, and it is located at a longitude of $277 \pm 6 \text{ deg}$ (measured counterclockwise from the line of star centers). This system is further analyzed in Sect. 4.1.1.
- M31V J00451973+4145048. A largely negative V third light contribution is observed. However, the resulting error is also very large due to the lack of observations at the bottom of the primary eclipse. Considering that the V light curve is the only data set having no observations at the bottom of the primary eclipse and that positive third light contributions are observed for the other light curves, the derived fundamental parameters are expected to be accurate.
- M31V J00444914+4152526. An equatorial hot spot was assumed for this EB system. The best fit yields a spot with a temperature ratio of 1.2, at a longitude of $246 \pm 14 \text{ deg}$ and a size of $17 \pm 3 \text{ deg}$.
- M31V J00442478+4139022. The large scatter of the DIRECT V light curve prevented a reliable fit from being achieved. Consequently, the DIRECT light curve was not used.
- M31V J00445935+4130454. A very slight O'Connell effect was observed in this EB system, suggesting the presence of a hot spot. The best fit, with a temperature ratio of 1.1, yields a spot at $280 \pm 60 \text{ deg}$ and a size of $21 \pm 11 \text{ deg}$.

The obtained values provide a good estimation of the potential of each EB system to become a good distance determination target. In general, the best targets should have low third light contribution and a luminosity ratio close to unity. On one hand, a strong third light contribution would lead to underestimating the

Table 2.3. Fundamental properties of the 24 EBs with W&D fits (see text for nomenclature). Targets selected for observation with GMOS at Gemini-North are highlighted.

Identifier	Cont. ^a	j_{mean}	P	i	e	ω	R_P/d^b	R_S/d^b	$T_{\text{atm},P}$	$(L_S/L_P)^b$	$(L_S/L_P)^c$	$(L_S/L_P)^d$	β_S^e	γ_S^e	ρ_S^e
[M31V]		[mag]	[days]	[deg]		[deg]									
J0044528+4128000	SD	18.854	11.543654±0.000211	78.0±1.3	0.0	—	0.556±0.009	0.277±0.002	0.453±0.033	0.0513±0.0003	0.0575±0.0004	0.0575±0.0004	0.0	0.0	0.0
J00435515+4124567	D	19.164	6.816191±0.000067	89.1±4.4	0.105±0.010	327.4± 7.8	0.160±0.007	0.281±0.012	0.911±0.018	2.69±0.09	2.70±0.08	2.70±0.08	0.055±0.030	-0.005±0.030	—
J00442326+4127082	D	19.242	5.752689±0.000037	87.3±2.4	0.189±0.019	51.3± 4.7	0.215±0.017	0.267±0.025	0.890±0.027	1.25±0.13	1.27±0.14	1.27±0.14	0.329±0.039	0.336±0.043	0.328±0.051
J00451253+4137261	SD	19.366	2.358359±0.000010	75.4±3.0	0.0	—	0.369±0.023	0.372±0.007	0.885±0.020	0.80±0.08	0.82±0.09	0.82±0.12	0.285±0.056	0.308±0.059	0.325±0.070
J00443799+4129236	SD	19.428	3.549696±0.000012	83.3±0.6	0.0	—	0.330±0.019	0.390±0.006	0.772±0.012	0.88±0.04	0.90±0.04	0.90±0.04	0.0	0.0	0.0
J00442928+4123013	SD	19.475	3.168969±0.000006	86.4±2.5	0.0	—	0.329±0.014	0.403±0.005	0.857±0.011	1.17±0.05	1.19±0.05	1.19±0.06	0.042±0.035	0.027±0.032	0.022±0.034
J00450486+4137291	SD	19.536	3.094681±0.000013	75.7±3.0	0.0	—	0.316±0.021	0.390±0.008	0.787±0.015	1.01±0.12	1.03±0.12	1.03±0.13	0.016±0.098	-0.041±0.093	-0.033±0.096
J00451973+4145048	D	19.572	8.130670±0.000087	87.2±2.4	0.252±0.027	109.1± 1.8	0.216±0.014	0.149±0.012	0.894±0.016	0.34±0.06	0.35±0.06	0.34±0.07	0.041±0.077	-0.136±0.096	0.115±0.096
J00450051+4131393	D	19.756	5.211976±0.000044	81.7±1.2	0.040±0.015	120.0±14.1	0.128±0.005	0.349±0.011	0.993±0.005	7.67±0.35	7.74±0.38	7.73±1.47	0.063±0.025	0.069±0.024	0.055±0.086
J00444914+4152526	SD	19.772	2.626992±0.000010	72.5±1.5	0.0	—	0.340±0.015	0.384±0.005	0.957±0.026	1.20±0.09	1.21±0.09	1.21±0.09	0.003±0.046	0.009±0.047	—
J00442478+4139022	D	20.034	4.762310±0.000068	79.9±1.2	0.027±0.008	188.8±33.4	0.105±0.003	0.333±0.014	0.848±0.004	7.48±0.34	7.65±0.35	7.65±0.35	0.0	0.0	—
J00443610+4129194	SD	20.038	2.048644±0.000006	70.6±1.7	0.0	—	0.290±0.018	0.369±0.007	0.946±0.020	1.51±0.18	1.52±0.18	1.52±0.18	0.067±0.034	0.051±0.032	0.016±0.047
J00425907+4136527	D	20.060	5.874724±0.000069	81.0±1.1	0.163±0.016	70.8± 2.2	0.344±0.013	0.157±0.011	1.046±0.021	0.22±0.02	0.22±0.02	0.22±0.02	0.053±0.017	0.051±0.029	0.034±0.023
J00425254+4145035	SD	20.090	5.009412±0.000047	82.3±3.4	0.0	—	0.247±0.020	0.393±0.008	0.810±0.018	1.72±0.13	1.78±0.13	1.78±0.27	0.169±0.014	0.162±0.023	0.227±0.029
J00442722+4136082	SD	20.098	4.518795±0.000016	86.1±1.7	0.0	—	0.308±0.018	0.344±0.009	0.747±0.008	0.72±0.05	0.76±0.05	0.76±0.06	0.109±0.009	0.130±0.010	0.119±0.014
J00453244+4147425	SD	20.141	2.787856±0.000010	78.4±1.7	0.0	—	0.238±0.012	0.342±0.007	0.728±0.009	1.14±0.11	1.20±0.12	1.20±0.17	0.036±0.022	0.018±0.026	0.093±0.090
J00445935+4130454	SD	20.166	2.668419±0.000023	68.1±1.9	0.0	—	0.277±0.025	0.347±0.013	0.857±0.063	1.22±0.24	1.25±0.25	1.25±0.25	0.169±0.079	0.219±0.082	—
J00450377+4133402	SD	20.326	1.769903±0.000005	75.4±2.5	0.0	—	0.351±0.025	0.350±0.010	0.940±0.015	0.88±0.10	0.89±0.10	0.89±0.13	-0.055±0.110	-0.027±0.102	-0.037±0.117
J00452610+4142010	SD	20.340	4.274429±0.000065	75.9±3.6	0.0	—	0.206±0.027	0.413±0.014	0.838±0.028	3.15±0.77	3.23±0.79	3.23±0.79	0.243±0.043	0.309±0.061	—
J00445682+4131109	D	20.360	4.207679±0.000036	87.2±4.5	0.0	—	0.345±0.015	0.158±0.015	0.891±0.024	0.18±0.03	0.18±0.03	0.18±0.04	0.118±0.076	0.129±0.087	0.153±0.117
J00453082+4121517	D	20.367	2.176672±0.000011	79.6±4.1	0.0	—	0.305±0.026	0.358±0.031	0.789±0.019	0.89±0.18	0.93±0.19	0.93±0.19	0.245±0.074	0.211±0.091	—
J00425743+4137114	SD	20.388	1.916302±0.000008	73.9±2.9	0.0	—	0.364±0.019	0.379±0.006	0.921±0.014	0.94±0.11	0.96±0.11	0.96±0.11	0.165±0.063	0.219±0.070	—
J00425929+4138169	D	20.450	5.591515±0.000045	85.5±4.0	0.0	—	0.340±0.011	0.264±0.016	0.548±0.011	0.17±0.02	0.19±0.02	0.19±0.02	0.195±0.042	0.203±0.049	0.139±0.045
J00445011+4128069	D	20.456	2.861046±0.000009	80.2±2.4	0.0	—	0.347±0.013	0.286±0.013	0.603±0.016	0.25±0.03	0.26±0.03	0.26±0.03	-0.012±0.090	-0.004±0.080	0.001±0.105

^aConfiguration. (D): Detached, (SD): Semi-detached.

^b R_P/a and R_S/a are the relative radii of the components, where a is the semi-major axis of the system.

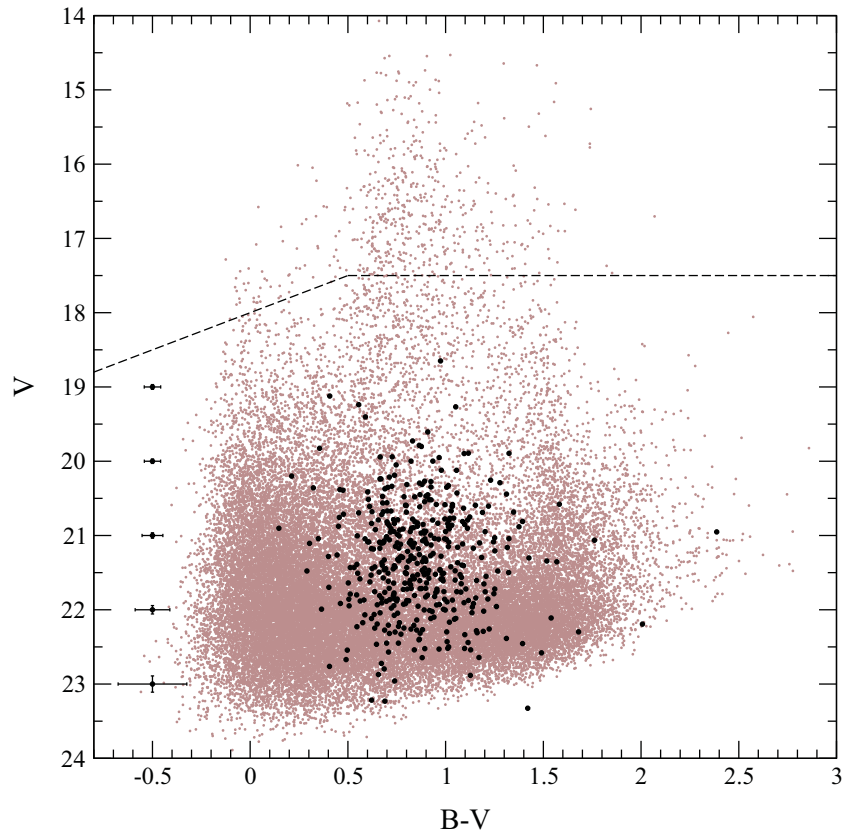


Figure 2.12. Color–magnitude diagram for 37 241 objects with photometric errors lower than 0.1 mag in both B and V in the reference catalog (gray dots) and 416 Cepheids (black circles). Stars above the dashed lines are saturated. Error bars on the left indicate the mean error, in magnitude and color, at different magnitude values.

observed standard magnitudes for the EB system. Although the third light can be modeled, the resulting values may have uncertainties that are large enough to have a sizeable negative effect on the accuracy of the distance determination (Wilson & Wyithe, 2003). On the other hand, EBs with luminosity ratios close to unity will have spectra with visible lines for the two components, thus making the determination of accurate fundamental properties possible.

2.4.2 Cepheids

Although the main targets of this work are EBs, the variable stars most commonly used for distance determination are Cepheids (Chap. 1). The visual inspection of the variable star catalog revealed a total amount of 416 Cepheids with ~ 250 measurements in both B and V passbands. The standard errors in the V (and $B - V$) passband range from 0.03 mag (0.04 mag) at $V \sim 19$ mag to 0.11 mag

(0.18 mag) at $V \sim 23$ mag (Fig. 2.12). As will be shown in Sect. 5.3.1, the line-of-sight absorption is computed from the observed color. Therefore, it is obvious that fainter Cepheids will have large uncertainties in their absolute magnitudes and will have low significance in the distance determination to M31. However, their periods are still very accurate and therefore, the full sample can be used to study the completeness and the presence of any possible bias (Sect. 5.1). So, the entire Cepheid sample was selected to determine the characteristics of the Cepheid population (Chap. 5).

